



Effect of Co on oxidation and hot corrosion behavior of two nickel-based superalloys under $\text{Na}_2\text{SO}_4\text{--NaCl}$ at 900 °C

Jun-sheng MENG, Ming-xuan CHEN, Xiao-ping SHI, Qiang MA

Naval Architecture and Port Engineering College, Shandong Jiaotong University, Weihai 264200, China

Received 14 August 2020; accepted 28 April 2021

Abstract: Nickel-based superalloys with and without Co by partial replacement of W were prepared using double vacuum melting. A comparison of the oxidation in air and hot corrosion behaviors under molten 75wt.% Na_2SO_4 +25wt.%NaCl at 900 °C were systematically investigated. The results showed that partial replacement of W with Co promoted the formation of chromia scale and consequently decreased the oxidation rate. Besides, the addition of Co also retarded the internal oxidation/nitridation of Al and consequently promoted the growth of Al_2O_3 scale, which further decreased the scaling rate and improved the adhesion of scale. Moreover, the addition of Co also further improved the hot corrosion resistance under molten $\text{Na}_2\text{SO}_4\text{--NaCl}$ salts.

Key words: nickel based superalloys; oxidation; hot corrosion; spallation resistance

1 Introduction

Nickel-based superalloys consisting of a continuously disordered γ matrix and ordered γ' precipitates are widely used in aircraft turbine engines and subjected to a highly aggressive environment, in which both good mechanical properties and high oxidation resistance are required [1,2]. Normally, the oxidation/corrosion resistances of Ni-based superalloys are primarily determined by the content of Cr/Al due to the thermally-induced growth of continuous protective $\text{Cr}_2\text{O}_3/\text{Al}_2\text{O}_3$ scales [3]. Compared to Cr_2O_3 scales, Al_2O_3 scales provide superior oxidation resistance at temperatures above 871 °C [4,5]. However, Cr_2O_3 exhibits better hot corrosion resistance in molten salts than Al_2O_3 [6].

Recently, different Ni-based superalloys containing 2–22 wt.% Cr and 1.5–10 wt.% Al with good oxidation performance were developed [7–9]. As the roles of Cr and Al are the most important,

the effects of other alloying elements have received less attention. However, the addition of other minor elements can significantly affect the oxidation resistance.

Alloying Co improves mechanical properties at high temperatures, but the effects of Co on oxidation behavior are unclear as different researchers have concluded differing results. For example, CHOI et al [10] indicated that the addition of Co could slightly increase the isothermal oxidation resistance of Ni_3Al base alloy but decreased the cyclic oxidation resistance at 1000–1200 °C. WEISER et al [11] reported that the replacement of Ni by Co in Ni–9Al–8W–8Cr (at.%) alloy enhanced the oxidation resistance at low temperatures (≤ 850 °C), but decreased the oxidation rate at 900 °C. ISMAIL et al [12] indicated that an increment in Co concentration decreased the oxidation performance of Co–Ni base superalloys at 800 °C. Therefore, the effect of Co on oxidation resistance is complex, and may be affected by other elements, environments, and

temperatures. However, the addition of Co can improve the hot corrosion resistance of Ni-based superalloys [10,13,14].

Mo and W are known to be the primary alloying elements which could improve the mechanical properties of Ni-based superalloys at high temperatures [15,16], but their effects on oxidation behavior are still unclear. PARK et al [4] found that Mo increased the oxidation rates of Ni–9.5Co–(8–12)Cr–(2.5–5.5)Mo–(4–8)W–3Al–5Ti–3Ta–0.1C–0.01B (wt.%) alloys in air at 850 °C, but decreased oxidation rates at 1000 °C. Furthermore, W slightly increased the mass gain at 850 °C but did not produce a significant effect at 1000 °C. However, PARK et al [17] found that the mass gain of the Ni–W–Cr alloys with low Cr (8 wt.%) decreased with increasing W content (0–10 wt.%). In an environment containing Na₂SO₄ salt, W and Mo are prone to cause an acid melting reaction. Meanwhile, the selective corrosion of α -W phases further decreases the corrosion resistance. Compared with Mo, W has stronger hot corrosion resistance. However, YUN et al [18] and PARK et al [4,17] found that the harmful effects of Mo and W can be suppressed by alloying sufficient concentrations of Cr and Al.

To balance the resistances to high temperature oxidation and molten salt corrosion, two Ni-based superalloys with Co (Alloy 1) and without (Alloy 2) were fabricated by the partial replacement of W. The content of W is 13.5 wt.% for Alloy 2 and 10.5 wt.% for Alloy 1, far below the solubility limit of W in nickel-based alloy to inhibit growth of the α -W phase. The content of Mo is 2.5 wt.%. The contents of Cr and Al are 15.5 wt.% and 4.5 wt.%, respectively, which is close to that of In738LC [19] and at the borderline between “chromia former” and “alumina former”, so even slight compositional changes lead to the different oxide scale structures and compositions [4,5].

In this work, a comparison of the oxidation/hot corrosion behavior of two Ni-based superalloys under molten 75wt.%Na₂SO₄+25wt.%NaCl at 900 °C were systematically investigated. The oxidation kinetics, scale morphology, and phase composition were analyzed in depth with a focus on the effects of partial replacement of W by Co on the oxidation/corrosion behavior of alloys.

2 Experimental

2.1 Materials preparation

Two ingots with and without Co were prepared by double vacuum melting using alloy powders supplied by the Research Institute of Nonferrous Metals (China) with 99.99 wt.% purity. The ingots were homogenized at 1200 °C for 2 h in flowing Ar and then aged at 900 °C for 50 h, followed by air-cooling. To determine the actual compositions, pieces of both alloys were dissolved and subsequently analyzed using inductively coupled plasma (ICP) spectroscopy, as listed in Table 1. Specimens with approximate dimensions of 8 mm × 8 mm × 3 mm were cut from the heat treated ingot, and polished to a 2000-grit SiC paper, then degreased in acetone, ultrasonically cleaned in alcohol, and finally dried in air.

Table 1 Chemical composition of two Ni-based superalloys (wt.%)

Alloy	Al	Cr	Co	Mo	W	Ni
1	4.56	15.67	3	2.43	10.51	Bal.
2	4.62	15.62	–	2.47	13.42	Bal.

2.2 Oxidation and hot corrosion test

Isothermal oxidation was carried out at 900 °C for 100 h in air. The samples were removed from the furnace after a required exposure time, air-cooled in air for approximately 15 min, and then weighed. Cyclic oxidation testing was performed in a horizontal furnace at 900 °C for 100 h. The samples were oxidized for 50 min and cooled in air for 10 min, which is, altogether, defined as one cycle. Hot corrosion was carried out under 75wt.%Na₂SO₄+25wt.%NaCl at 900 °C with a thin salt layer of 1.2 mg/cm². After certain durations, the specimens were removed, cleaned in boiling water, and dried in hot air, weighed, and re-painted for further testing. The complete time for the hot corrosion was 40 h. Mass changes of specimens after oxidation/hot corrosion were measured after fixed time intervals using an electronic balance with an accuracy of 0.01 mg.

After oxidation/hot corrosion, the phase, surface and cross-sectional morphologies of scales formed were characterized using D/Max-2500 pc type X-ray diffraction (XRD) and Camscan

MX2600FE type scanning electron microscopy with energy dispersive spectrometry (SEM/EDS, Oxford Instruments, INCA).

3 Results

3.1 Microstructure

The microstructures of the both alloys after heat-treatment are shown in Fig. 1. Both alloys primarily consist of a disordered γ matrix and uniformly ordered cuboidal γ' phase. According to previous results [9,15,16], increasing W content will refine the grains as W can reduce the γ' -precipitate growth and coarsening at elevated temperatures. However, Fig. 1 indicates that both alloys exhibit a comparable grain size. The average edge length of the γ' phase for both alloys is $\sim 0.175 \mu\text{m}$, suggesting that minor partial replacement of W by Co has no effect on the grain refinement.

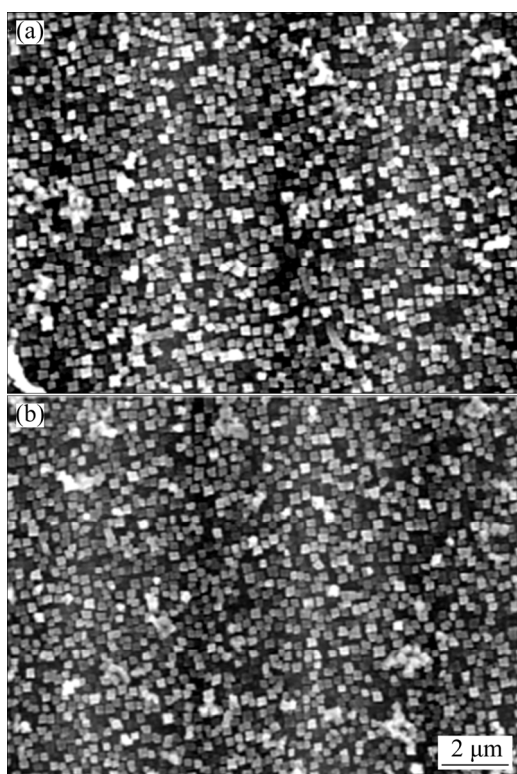


Fig. 1 Microstructures of Alloy 1 (a) and Alloy 2 (b)

3.2 Isothermal oxidation

Figure 2(a) shows the isothermal-oxidation kinetics curves of both samples in air at 900°C for 100 h. During oxidation and cooling, no visible spallation occurred for both alloys. Compared to Alloy 2, Alloy 1 exhibited an apparently lower

scaling rate over the course of the entire oxidation process. From the corresponding parabolic plots (Fig. 2(b)), oxidation can be divided into two stages: an initial transient stage and a steady-state stage. The calculated parabolic oxidation rate constants are also shown in Fig. 2(b). Clearly, Alloy 1 exhibited a lower oxidation rate, even at the beginning of oxidation.

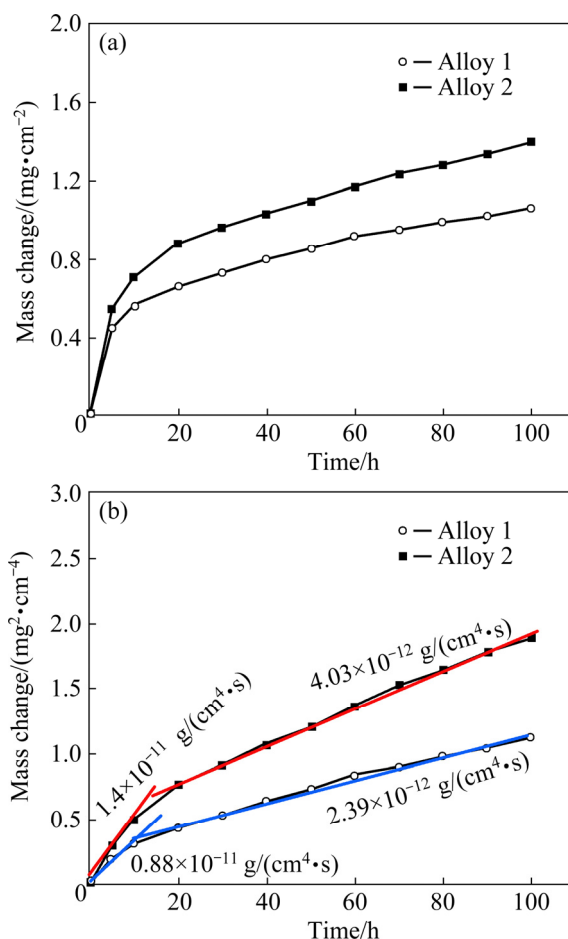


Fig. 2 Isothermal-oxidation kinetics curves (a) and corresponding parabolic plots (b) of different alloys at 900°C in air for 100 h

The oxide phases formed on both samples after 100 h isothermal oxidation at 900°C were characterized using XRD, as seen in Fig. 3. This result indicated that the oxide scales formed on Alloy 2 were primarily composed of Cr_2O_3 with minor NiO and $\alpha\text{-Al}_2\text{O}_3$. However, comparable Cr_2O_3 and $\alpha\text{-Al}_2\text{O}_3$ with minor NiO formed on Alloy 1. This result demonstrated that the partial replacement of W by Co significantly promoted the growth of $\alpha\text{-Al}_2\text{O}_3$. As the scales are thin, the diffraction patterns of the Ni-based superalloys were also detected, especially for Alloy 1.

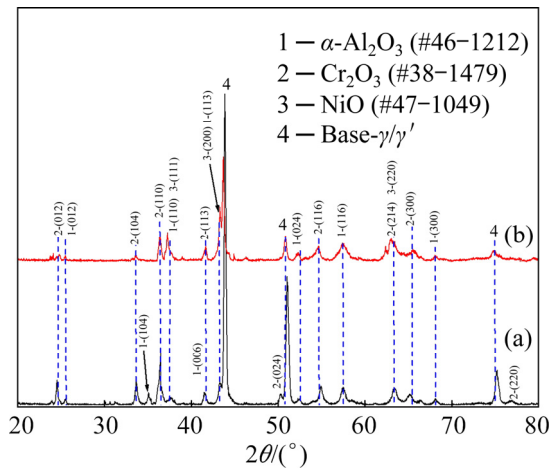


Fig. 3 XRD patterns of Alloy 1 (a) and Alloy 2 (b) after isothermal-oxidation at 900 °C for 100 h

The surfaces of both samples after isothermal oxidation at 900 °C for 100 h in air were further investigated by SEM. Two different morphologies were observed on both alloy surfaces, namely compact fine-grain crystalline (Region 1) and porous coarse-grain crystalline (Region 2), as presented in Fig. 4. EDS results indicated that the oxides in Region 1 contained Cr and O with minor levels of Ni, which are shown to be Cr_2O_3 with minor NiO, according to the XRD results shown in Fig. 3. However, the oxides in Region 2 primarily contained Ni and O with minor Cr. Therefore, it was

determined that NiO formed on the top of the Cr_2O_3 oxides. As shown in Figs. 4(a) and (c), it can be found that the surface area covered by Cr-rich oxides on Alloy 1 is higher than that on Alloy 2. This implies that the time to formation of a continuous protective Cr-rich oxide layer on Alloy 1 is shortened, which can also be described as less NiO formed on Alloy 1. This coincides well with the XRD analysis, which shows that the scale on Alloy 1 is mainly composed of Cr_2O_3 and Al_2O_3 .

Figure 5 shows the cross-sectional SEM images of Alloy 1 after isothermal oxidation at 900 °C for 100 h in air. The oxide scale on Alloy 1 ranges from ~ 7 to ~ 15 μm in thickness, and two different morphologies were observed with and without internal oxidation (Fig. 5(a)). Figures 5(b) and (c) are the higher magnification views of Region A and Region B in Fig. 5(a), respectively. In Region B without internal oxidation, the oxide scales appeared as light gray, dark thick gray, and black thin gray from outer to inner and are correspondingly labeled as 1, 2 and 3 in Fig. 5(c). In Region A, the dark gray layer connects with Layer 2 in Fig. 5(c). Moreover, the black strip-like gray internal layer almost forms a continuous black gray layer, and connects with Layer 3 in Fig. 5(c). Above the dark gray layer, minor light oxides are dispersed (Fig. 5(b)).

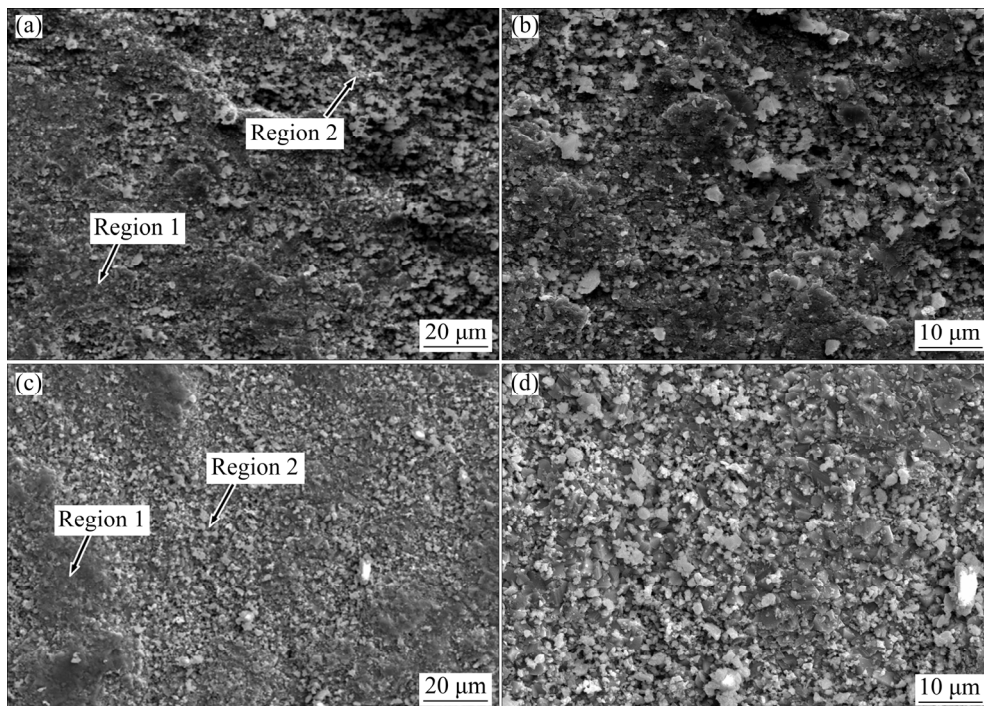


Fig. 4 Surface morphologies of Alloy 1 (a, b) and Alloy 2 (c, d) after isothermal-oxidation at 900 °C for 100 h

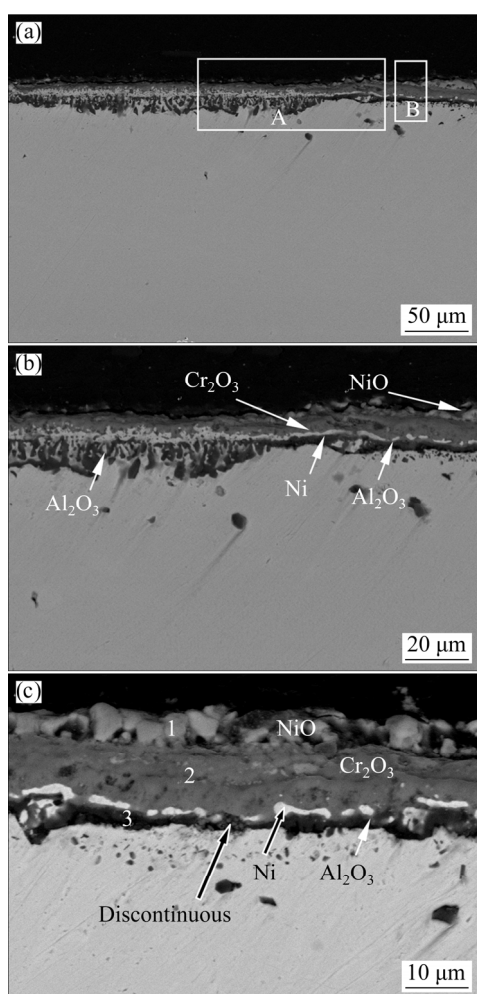


Fig. 5 Cross-sectional morphologies of Alloy 1 after isothermal-oxidation at 900 °C for 100 h: (a) SEM image of Alloy 1; (b) Enlargement of Area A; (c) Enlargement of Area B

The above results indicated that a three-layer scale formed on Alloys 1. Table 2 presents the compositions of the three oxide layers on Alloy 1 based on a basis of EDS analysis.

Layer 1 is a Ni-rich oxide with Co (4.3 wt.%) and Cr (3.5 wt.%), and Layer 3 is an Al-rich oxide with minor Ni, Cr, and Co. Layer 2, between layers 1 and 3, is a Cr-rich oxide. It is noteworthy that the thicknesses of Layer 1 and Layer 3 are less than the

2 μm EDS beam diameter. In other words, the EDS measurement integrated some of Cr from Layer 2 (Cr-rich oxide) into Layer 1 while that from the substrate superalloy into Layer 3. Figure 5 also indicates that some bright Ni-rich phases appeared between Layer 2 and Layer 3. Furthermore, the bright Ni-rich phases even form a continuous layer in Region A. EDS mapping of scales indicated the oxide scale consisted of a Ni-rich oxide outer layer, Cr-rich middle layer, and Al-rich inner layer. The bright phases between Cr-rich layer and Al-rich layer are Ni-rich without O. Base on the above results, it can be assumed that Layer 1 is NiO, Layer 2 is mainly Cr₂O₃ and Layer 3 is mainly Al₂O₃. The bright phases between Layer 2 and Layer 3 are Ni without oxidation. Furthermore, the Al₂O₃ scale in region B is also discontinuous. From the above results, it can be found that a continuous porous NiO layer formed on the surface without internal oxidation, but minor NiO particles disperse on the surface with internal oxidation (Fig. 5(c)). This also coincides well with surface SEM results in Fig. 4 and XRD results in Fig. 3.

Figure 6 shows cross-sectional morphologies of scales formed on Alloy 2 after isothermal oxidation at 900 °C for 100 h in air. Clearly, Alloy 2 also formed a similar three-layer scale as that formed on Alloy 1, as seen in Figs. 6(b) and (c). The compositions of the three layers on Alloy 2, labeled with 1, 2 and 3, in Fig. 6(c) are also presented in Table 2. The results indicate that the oxide scales formed on Alloy 2 have a similar content and exhibit similar trends in chemical composition variation from the oxide surface to the oxide/underlying substrate interface as that formed on Alloy 1. In other words, both Ni-based superalloys formed a similar three-layer scale. However, compared to Alloy 1, Alloy 2 formed a rougher and thicker oxide scale with a thickness from ~12.3 to ~19.3 μm. Furthermore, the internal Al₂O₃ could not form a continuous Al₂O₃ layer in some regions on Alloy 2, as seen in Fig. 6(c).

Table 2 Compositions of oxide layers by EDS on two Ni-based superalloys after 100 h isothermal-oxidation at 900 °C in air (at.%)

Alloy No.	Layer 1					Layer 2					Layer 3				
	O	Al	Cr	Ni	Co	O	Al	Cr	Ni	Co	O	Al	Cr	Ni	Co
1	45.7	0.2	3.5	47.3	4.3	58.8	0.2	37.2	3	0.8	56.3	30.6	3.5	10	2.6
2	44.4	0.3	4.8	50.5		57.5	0.3	36.4	2.8		53.8	28.8	4.8	12.6	

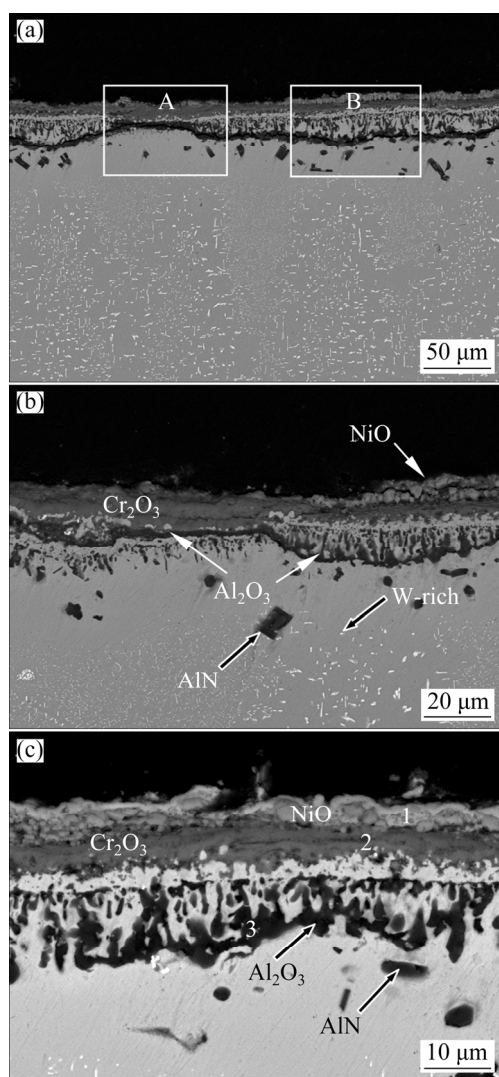


Fig. 6 Cross-sectional morphologies of Alloy 2 after isothermal-oxidation at 900 °C for 100 h: (a) Cross-sectional SEM image of Alloy 2; (b) Enlargement of Area A; (c) Enlargement of Area B

From Figs. 5 and 6, it can be found that time for the formation of the more protective Al_2O_3 layer was prolonged on Alloy 2, thus a higher oxidation rate was observed. It can be found that significant voids formed at the outer NiO/middle Cr_2O_3 interface, suggesting loose contact with the Cr_2O_3 middle layer. In addition, it should be noted that minor and significantly dark precipitates appeared below the scales on Alloy 1 and Alloy 2, respectively. The precipitates are Al-rich without oxygen. Based on previous works [20], AlN precipitates. Furthermore, at a distance beneath the internal alumina, about 20 μm of bright W-rich fine particles appear on Alloy 2 due to the solubility limit of W or the coarsening of initial fine W-rich

phases formed during oxidation, which needs further investigation. However, the appearance of the $\sim 20\ \mu\text{m}$ thick zone without W-rich phases below the internal Al_2O_3 indicates that the degradation of γ' to γ is attributed to the outward diffusion of Cr and Al significantly increasing in W in this region [14,21].

3.3 Cyclic oxidation

The mass change with time curves of cyclic oxidation of both samples in air at 900 °C are shown in Fig. 7. For the first 30 h cyclic oxidation, no scale spallation occurred in both alloys, and the mass gain is comparable to that in Fig. 2. For Alloy 2, significant mass loss occurred at 40 h due to severe spallation, which could also be observed by the naked eye.

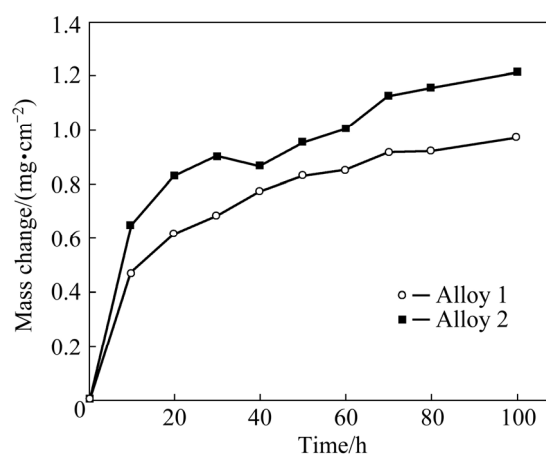


Fig. 7 Mass changes of alloys during cyclic-oxidation at 900 °C for 100 h in air

After that the mass gain steadily increased, suggesting that repeated spallation resulted in the regrowth of less protective scale on the spallation area. However, during the 100 h cyclic oxidation period, no significant mass gain or mass loss occurred for Alloy 1, indicating a better cyclic oxidation resistance. XRD characterization indicated that the oxides formed on both samples were also composed of Cr_2O_3 and Al_2O_3 with minor NiO, like that formed at isothermal oxidation. However, the NiO peaks intensities were much weaker, suggesting less NiO formed or spallation of NiO oxides during the thermal cycling, which was also visually confirmed by SEM/EDS.

Figures 8 and 9 show the surface and corresponding cross-sectional morphologies of both alloys after cyclic-oxidation at 900 °C for 100 h.

Clearly, minor spallation occurred on Alloy 1 (Fig. 8(a)). However, heavy spallation occurred on Alloy 2, as seen in Fig. 9(a). In the spallation area, new porous coarse-grain oxides as outward protrusions formed on both alloys, especially for

Alloy 2.

From the corresponding cross-sectional morphologies shown in Figs. 8(c,d) and Figs. 9(c,d), it can be found that both alloys formed a similar three-layer scale as that observed during

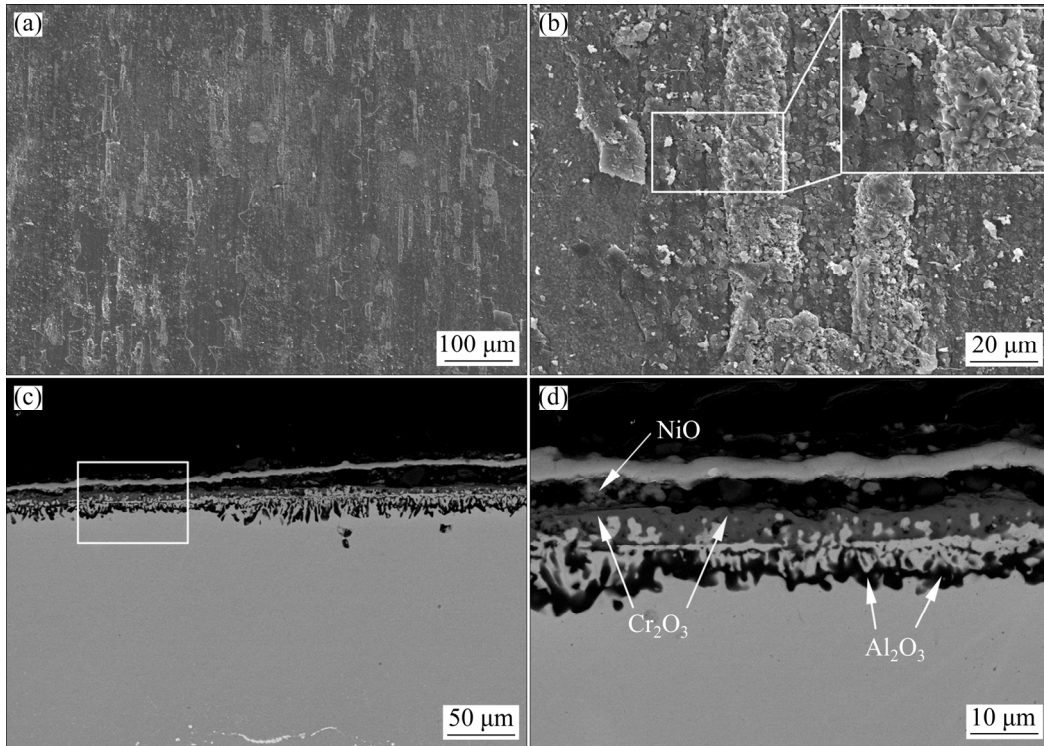


Fig. 8 Surface (a, b) and cross-sectional (c, d) morphologies of Alloy 1 after cyclic-oxidation at 900 °C for 100 h

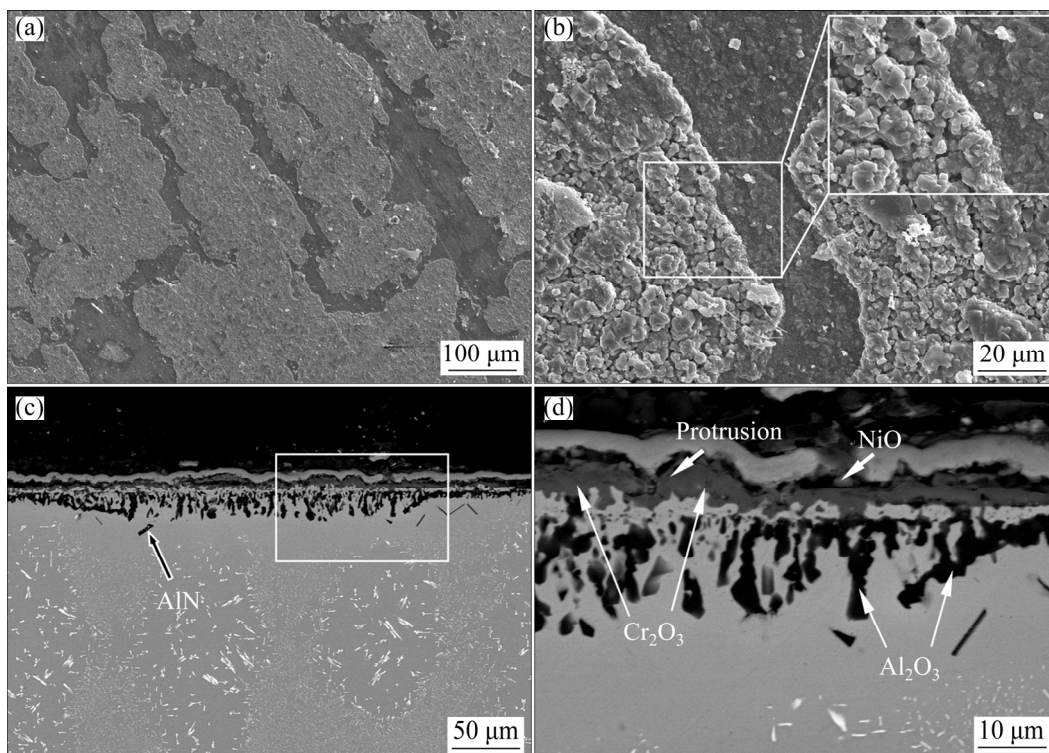


Fig. 9 Surface (a, b) and cross-sectional (c, d) morphologies of Alloy 2 after cyclic-oxidation at 900 °C for 100 h

isothermal oxidation. For Alloy 1, the inner Al_2O_3 aggregates almost link together to form a continuous Al_2O_3 inner layer (Fig. 8(d)). However, the inner Al_2O_3 aggregates could not form a continuous Al_2O_3 inner layer in some regions on Alloy 2, as seen in Fig. 9(d). In these regions, a thicker Cr_2O_3 ($\sim 4.5 \mu\text{m}$) layer formed due to the growth of outward protrusions, which is consistent with the surface SEM results in Fig. 9(b).

3.4 Hot-corrosion

Figure 10 illustrates the mass change vs time curves for both samples at 900°C in mixed salts of 75wt.% Na_2SO_4 +25wt.% NaCl . The mass change consists of a mass gain from the scale formation plus a mass loss by the scale spallation and dissolution. A comparable mass change occurs in the first 10 h, and then different behaviors occurs. For Alloy 1, the mass change steadies for the first 20 h, and then undergoes a fast increase till 40 h. However, the mass change of Alloy 2 starts to decrease after 10 h, and the mass loss even surpasses the mass gain at 20 h.

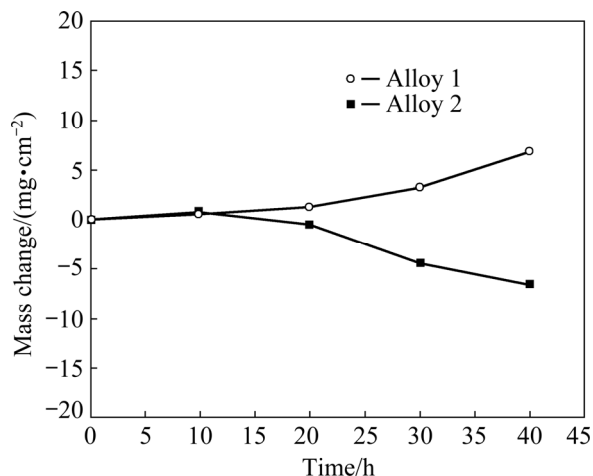


Fig. 10 Curves of mass change vs time of sample exposed in air at 900°C for 40 h in salt of 75wt.% Na_2SO_4 +25wt.% NaCl

Figure 11 shows the cross-sectional morphologies of corrosion scales formed on Alloy 1 after hot corrosion at 900°C for 40 h in mixed salts of 75wt.% Na_2SO_4 + 25wt.% NaCl . Obviously, Alloy 1 formed a thin ($\sim 30 \mu\text{m}$), compact, uniform, and adherent scale in most regions, with minor internal corrosion, as seen in Fig. 11(b). In some regions, a $\sim 100 \mu\text{m}$ thick scale with voids/minor detachment at the scale/underlying substrate interface occurred.

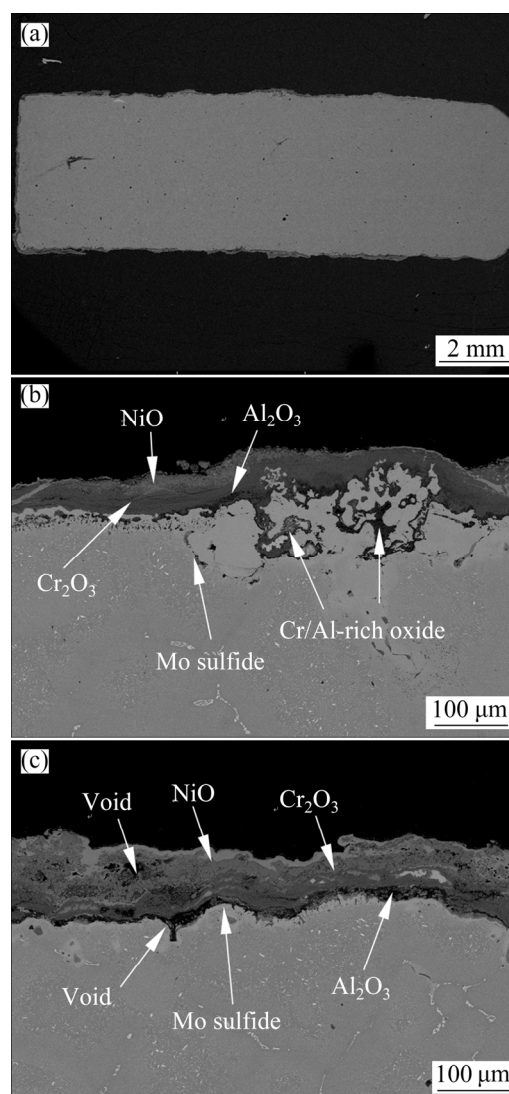


Fig. 11 Cross-sectional morphologies with different magnifications of Alloy 1 after corrosion at 900°C for 40 h in salts of 75wt.% Na_2SO_4 +25wt.% NaCl

Even so, the scales can be divided into three layers from outer to inner, which were the same as that during oxidation. EDS mapping results indicated that the porous outer layer is NiO, the middle compact continuous layer is Cr_2O_3 , and the inner discontinuous layer is Al_2O_3 . Below the thinner scale, internal oxidation of Cr/Al and internal sulfidation of Mo occurred (Fig. 11(b)). However, sulfides of Mo and white un-oxidized Ni-rich phases occurred in the lower part of the thicker scale (Fig. 11(c)), indicating inward growth of corrosion scale. In contrast, for Alloy 2, severe spallation occurred, as seen in Fig. 12. Even so, a mixed internal corrosion scale in thickness from ~ 30 to $\sim 110 \mu\text{m}$ still formed on the alloy surface.

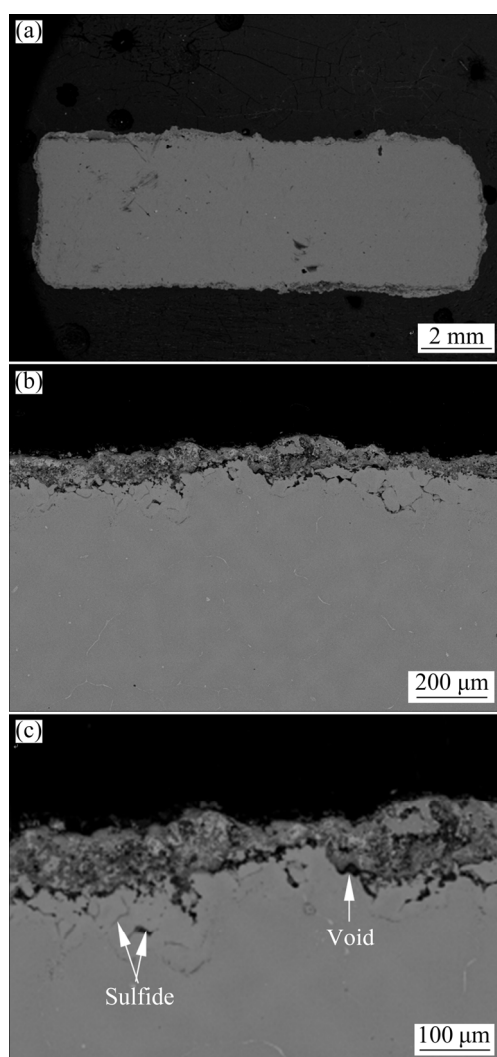


Fig. 12 Cross-sectional morphologies with different magnifications of Alloy 2 after corrosion at 900 °C for 40 h in salts of 75wt.%Na₂SO₄+25wt.%NaCl

Furthermore, the scale is porous with voids at the scale/underlying substrate interface. EDS mapping further indicates that the mixed scale was composed of an outer NiO and a discontinuous mixed inner layer of Cr₂O₃/Al₂O₃, which could not be clearly distinguished. Beneath the internal oxidation zone, significant internal sulfidation of Mo, Cr and Al occurred. Furthermore, sulfides were also observed in the lower part of the scale owing to inward growth of corrosion scale.

4 Discussion

4.1 High temperature oxidation

The oxidation mechanisms of Ni–Cr–Al alloys under steady-state conditions are normally divided into three types [18–20]. Type I is an external NiO

scale with Cr₂O₃ and/or Al₂O₃ internal oxides. Type II is an external layer of Cr₂O₃ with internal Al₂O₃ oxides. Type III is a continuous external Al₂O₃ layer with the best high-temperature corrosion resistance.

The results in this work confirm that both samples can form a continuous chromia scale at 900 °C, with certain amounts of NiO above and strip-like Al₂O₃ internal aggregates. The formation of NiO suggests that there exists a relatively long transient oxidation stage, during which NiO grows at a faster rate before the formation of a continuous chromia scale. From Figs. 3 to 9, it was observed that the chromia scale formed on Alloy 1 is much pure; namely, the formation of NiO is greatly suppressed. Therefore, it can be concluded that the addition of Co promotes the growth of chromia scale, and the reasons are addressed below.

At the initial stage of oxidation, the oxidation of Ni/Co, Cr, and Al took place, leading to the formation of NiO/CoO, Cr₂O₃, and Al₂O₃ nuclei. After NiO/CoO, Cr₂O₃, and Al₂O₃ nuclei covered the surface [3,18–20], the effective oxygen partial pressure at the alloy–oxide interface decreased to a level that it is unable to further oxidize Ni/Co. Cr and Al that have high affinities to oxygen could be easily oxidized [3–11]. Normally, the interdiffusion coefficient of Cr in Co base alloy is lower than that in Ni base alloy at temperature ≥ 900 °C [22], therefore the addition of Co decreased the outward diffusion of Cr to the oxidation front, thus decreasing the oxidation resistance [11]. Moreover, addition of Co increased the oxidation rate of alloys because Co is more easily oxidized than Ni [12]. Therefore, a higher oxidation rate normally occurs with the addition of Co. However, previous works [22] indicated that the diffusion coefficient of Cr in Co exceeds the same value for Ni at low temperatures (≤ 850 °C); therefore, the addition of Co increases the outward diffusion of Cr to the oxidation front and enhances the oxidation resistance at low temperatures (≤ 850 °C) [11]. Furthermore, the addition of Co increases the Cr content in γ matrix as a result of the increased γ' fraction [23]. Moreover, the initial fast outward diffusion of Co due to oxidation also increased the Cr content below scale [11]. All of them are believed to favor the growth of a continuous Cr₂O₃ scale on Alloy 1 in a short transient stage. The formation of a continuous chromia scale blocked the growth of NiO/CoO at the surface; therefore, a

lower oxidation rate occurred on Alloy 1. However, before the formation of a continuous chromia scale, the internal oxidation of Al caused the formation of strip-like discontinuous Al_2O_3 aggregates to deep into the substrate on some regions, especially for Alloy 2. With the growth of chromia scale, the oxygen partial pressure at the chromia scale/underlying substrate interface further decreased. The selective oxidation of Al started, therefore, a continuous Al_2O_3 layer formed at some locations (Fig. 5(c) and Fig. 6(b)). At the same time, the strip-like Al_2O_3 internal aggregates also began to link together to form a discontinuous/continuous Al_2O_3 layer in other areas (Fig. 5(b) and Fig. 6(c)).

Comparing the oxidation scales of both alloys, it can be further found that a thinner depth of internal Al_2O_3 oxides zone occurred on Alloy 1. Furthermore, the strip-like Al_2O_3 internal aggregates formed on Alloy 1 are more prone to form a continuous layer. These imply that the addition of Co also slightly promoted the growth of Al_2O_3 through the third elemental effect [10,13,14]. According to an initial suggestion by WAGNER [24], the third element, such as Cr, Co, and Ti, acts as an oxygen scavenger in the alloy during the initial stages, lowers the oxygen solubility in the alloy, and promotes the establishment of protective Al_2O_3 layers. The mechanism of the third element effect is not yet clear, but some ideas include: inhibition of internal oxidation of Al [24], complete solubility between Al_2O_3 and Cr [25,26], and inhibition of the growth of external oxides [27]. In general, Al_2O_3 scales provide a better protection against nitrogen and oxygen penetration than that of chromia scale. Owing to a long transient stage on Alloy 2, heavy internal oxidation and internal nitridation occurred, which also increased the oxidation rate.

The results in this work also show that the scale formed on Alloy 1 is highly adherent. It is well known that scale spallation is driven by the strain energy in the scale and resisted by the interfacial toughness [28]. The elastic strain energy (G) in the scale can be expressed as [28]

$$G = \frac{\sigma^2 h_{\text{ox}} (1 - \nu_{\text{ox}}^2)}{2E_{\text{ox}}} \quad (1)$$

where σ , h_{ox} , ν_{ox} and E_{ox} are the residual stress, the thickness, Poisson ratio, and elastic modulus of the scale, respectively. According to the equation

above, the driving force for spallation increases linearly with scale thickness, thus a lower scale growth rate will result in lower driving force for spallation. In most cases, the interfacial toughness degrades as result of the formation of large interfacial cavities due to the condensation of excess cation vacancies at the scale/underlying substrate interface, either from the growing scale or from the substrate due to the Krikendall effect. Normally, a higher oxidation rate always develops more interfacial voids. From this work, it was found that a higher oxidation rate and a thicker scale formed on Alloy 2 than on Alloy 1; therefore, a higher driving force for spallation and a more interfacial voids occurred for Alloy 2. Thus, poor scale adhesion occurred on Alloy 2. Moreover, the significant internal oxidation and internal nitridation of Al on Alloy 2 further decreased the scale adhesion by decreasing the mechanical properties of the alloys and producing embrittlement in the near-surface, due to their higher specific volume compared to the base alloy. After the thicker scale with surface NiO oxides (Fig. 6(c)) spalled locally, a fresh chromia scale regenerated through the outward diffusion of Cr to form large Cr_2O_3 protrusion, as seen in Fig. 9(b). That is why a pure chromia scale with less NiO formed on both alloys after cyclic oxidation, especially for Alloy 2.

4.2 Hot corrosion

Hot corrosion can be regarded as an accelerated oxidation induced by the deposited salts, such as sulfates and/or chlorides. At the onset of corrosion, a less protective NiO layer with many defects, such as pores and microcracks, formed on both Ni-based superalloys. The defects in NiO layer make it feasible that the molten salts penetrate the scale and reach the scale/alloy interface, where SO_4^{2-} is reduced there by the following chemical equilibrium:



The released S diffuses into the alloy and attacks the alloy, leading to internal sulfidation. This sulfidation causes a reduction in S activity and an increase in O^{2-} activity, resulting in basic fluxing of the NiO scale by the following reaction:



The dissolution of NiO again decreases the O^{2-} activity, which further increases the S activity. As a negative gradient of the O^{2-} activity exists across the fused salt layer, the dissolution of NiO at the salt/scale interface and the re-precipitation of NiO at the gas/salt interface can be sustained. Therefore, a porous NiO outer layer formed on both alloys. With corrosion, Cr- and Al-rich oxides are progressively formed below the NiO layer, which may significantly mitigate the continuous salt attack. However, for Alloy 2, because of a less ability to form a continuous protective scale of chromia, the attack of molten salts still causes the basic dissolution of Al_2O_3 particles by the following reaction:

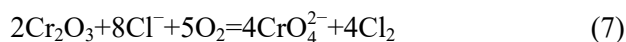
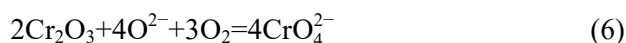


When NaCl is introduced into the salts films, hot corrosion is accelerated because the major role of NaCl is to crack or break the protective oxide scale as well as to generate the numerous pits and voids at the grain boundaries by means of oxychlorination and chlorination/oxidation cyclic reactions, resulting in additional dissolution of the Al_2O_3 oxides [13,29]:



The formed Cl_2 diffused inward across the loose oxide scales and reacted with Cr/Al in the substrate, resulting in the formation of $CrCl_3/AlCl_3$, which further reacted with O_2 to form their corresponding oxides, therefore accelerating alloy corrosion. In this case, a mixed scale of Cr_2O_3/Al_2O_3 with less protection formed on Alloy 2. The mixed scale formed on Alloy 2 could easily spall due to stress formed by thermal cycling and oxide growth. Both of dissolution of Al_2O_3 and spallation of mixed scale could significantly destroy the integrity of the scale, and result in the depletion of Cr/Al reservoir. In this case, the molten salt directly contacts with a greatly depleted alloy that is unable to reform a protective scale and a catastrophic attack starts. Therefore, after the spallation of corrosion scale, only an internal oxidation zone with lower internal sulfidation zones still contacted with the alloy (Fig. 12). The formed sulfides can further react with oxygen to form the corresponding oxides, thus driving the sulfur further into alloy. In this case, the sulfuration/oxidation cyclic reactions occurred and the alloy was repeatedly attacked by sulfur.

For Alloy 1, the addition of Co promoted the fast formation of a continuous chromia scale, as addressed in Section 4.1. Chromia is the best oxide to resist hot corrosion in molten salt, because it preferentially reacts with O^{2-} in molten salts to form chromate by



The chromate stabilizes the melt chemistry, and consequently prevents the dissolution/re-precipitation of the protective oxide scale. As corrosion progresses, the fast formation of a continuous compact Al_2O_3 scale beneath the chromia scale through the third element effect of Co further decreased the oxidation/corrosion of Alloy 1, since the layer could isolate the alloys from oxygen or other aggressive media. In addition, the diffusion rate of S in Ni is higher than that of sulfur in Co. So, the addition of Co could effectively reduce the internal diffusion of sulfur. Consequently, the sulfuration/oxidation cyclic reactions could be effectively alleviated. Furthermore, the addition of Co also improved the hot corrosion because the CoS as well as Co– Co_xS_y eutectic (such as Co– Co_4S_3 , 877 °C) are stable and have higher melting points than those of Ni (such as Ni– Ni_3S_2 , 645 °C) [30].

5 Conclusions

- (1) The addition of Co promoted the growth of a continuous chromia and consequently decreased the oxidation rate through the increment of Cr content below oxide scale and the enhanced outward diffusion of Cr to the oxidation front.
- (2) The addition of Co retarded the internal oxidation/nitridation of Al and thereby promoted the growth of Al_2O_3 scale through the third element effect, which further decreased the oxidation rate and improved the scale spallation resistance.
- (3) Co restrained the internal diffusion of sulfur, which therefore improved the hot corrosion resistance under molten 75wt.% Na_2SO_4 + 25wt.%NaCl salts.

Acknowledgments

The authors are grateful for the financial supports from the Natural Science Foundation of Shandong Province, China (No. ZR2019MEE107),

Shandong Jiaotong University “Climbing” Research Innovation Team Program, China (No. SDJTC1802), and PhD Scientific Research Foundation of Shandong Jiaotong University, China (No. BS2018005).

References

- [1] WU Yu-xiao, ZHANG Heng, LI Fu-lin, LI Shu-suo, GONG Sheng-kai, HAN Ya-fang. Kinetics and microstructural evolution during recrystallization of a Ni₃Al-based single crystal superalloy [J]. Transactions of Nonferrous Metals Society of China, 2012, 22: 2098–2105.
- [2] ZHOU Peng-jie, YU Jin-jiang, SUN Xiao-feng, GUAN Heng-rong, HU Zhuang-qi. Roles of Zr and Y in cast microstructure of M951 nickel-based superalloy [J]. Transactions of Nonferrous Metals Society of China, 2012, 22: 1594–1598.
- [3] MENG Jun-sheng, JI Ze-sheng. Effect of La₂O₃/CeO₂ particle size on high-temperature oxidation resistance of electrodeposited Ni–La₂O₃/CeO₂ composites [J]. Transactions of Nonferrous Metals Society of China, 2014, 24: 3571–3577.
- [4] PARK S J, SEO S M, YOO Y S, JEONG H W, JANG H J. Effects of Cr, W, and Mo on the high temperature oxidation of Ni-based superalloys [J]. Materials, 2019, 12: 2934.
- [5] MENG Jun-sheng, JI Ze-sheng. Effect of different fillers on oxidation behavior of low-temperature chromizing coating [J]. Transactions of Nonferrous Metals Society of China, 2014, 24: 1785–1790.
- [6] NATH M, GHOSH A, TRIPATHI H S. Hot corrosion behavior of Al₂O₃–Cr₂O₃ refractory by molten glass at 1200 °C under static condition [J]. Corrosion Science, 2016, 102:153-160.
- [7] PEDRAZZINI S, CHILD D J, WEST G, DOAK S S, HARDY M C, MOODY M P, BAGOT P A J. Oxidation behaviour of a next generation polycrystalline Mn containing Ni-based superalloy [J]. Scripta Materialia, 2016, 113: 51–54.
- [8] SABER D, EMAM I S, ABDEL-KARIM R. High temperature cyclic oxidation of Ni based superalloys at different temperatures in air [J]. Journal of Alloys and Compounds, 2017, 719: 133–141.
- [9] ZHANG Y B, HU X Y, LI C R, XU W W, ZHAO Y T. Composition design, phase transitions of a new polycrystalline Ni–Cr–Co–W base superalloy and its isothermal oxidation dynamics behaviors at 1300 °C [J]. Materials & Design, 2017, 129: 26–33.
- [10] CHOI S C, CHO H J, LEE D B. Effect of Cr, Co, and Ti additions on the high-temperature oxidation behavior of Ni₃Al [J]. Oxidation of Metals, 1996, 46: 109–127.
- [11] WEISER M, GALETZ M C, CHATER R J, VIRTANEN S. Growth mechanisms of oxide scales on two-phase Co/Ni-base model alloys between 800 °C and 900 °C [J]. Journal of The Electrochemical Society, 2020, 167: 021504.
- [12] ISMAIL F B, VORONTSOV V A, LINDLEY T C. Alloying effects on oxidation mechanisms in polycrystalline Co–Ni base superalloys [J]. Corrosion Science, 2017, 116: 44–52.
- [13] QIAO M, ZHOU C G. Hot corrosion behavior of Co modified NiAl coating on nickel base superalloys [J]. Corrosion Science, 2012, 63: 239–245.
- [14] FAN Q X, JIANG S M, WU D L, GONG J, SUN C. Preparation and hot corrosion behaviour of two Co modified NiAl coatings on a Ni-based superalloy [J]. Corrosion Science, 2013, 76: 373–381.
- [15] RAZUMOVSKIY V I, LOZOVIC A Y, RAZUMOVSKII I M. First-principles-aided design of a new Ni-base superalloy: Influence of transition metal alloying elements on grain boundary and bulk cohesion [J]. Acta Materialia, 2015, 82: 369–377.
- [16] SUDBRACK C K, ZIEBELL T D, NOEBE R D, SEIDMAN D N. Effects of a tungsten addition on the morphological evolution, spatial correlations and temporal evolution of a model Ni–Al–Cr superalloy [J]. Acta Materialia, 2008, 56: 448–463.
- [17] PARK S J, SEO S M, YOO Y S, JEONG H W, JANG H J, ZHNAG J. Statistical study of the effects of the composition on the oxidation resistance of Ni-based superalloys [J]. Journal of Nanomaterials, 2015, 11: 1–11.
- [18] YUN D W, SEO S M, JEONG H W, YOO Y S. Effect of refractory elements and Al on the high temperature oxidation of Ni-base superalloys and modelling of their oxidation resistance [J]. Journal of Alloys and Compounds, 2017, 710: 8–19.
- [19] GUO C, YU Z R, LIU C, LI X G, ZHOU Q, MARK WARD R. Effects of Y₂O₃ nanoparticles on the high-temperature oxidation behavior of IN738LC manufactured by laser powder bed fusion [J]. Corrosion Science, 2020, 171: 108715.
- [20] HUANG L, SUN X F, GUANE H R, HU Z Q. Oxidation behavior of the single-crystal Ni-base superalloy DD32 in air at 900, 1000, and 1100 °C [J]. Oxidation of Metals, 2006, 65: 391–408.
- [21] POPOVIC J, BROZ P, BURSİK J. Microstructure and phase equilibria in the Ni–Al–W system [J]. Intermetallics, 2008, 16: 884–888.
- [22] POPOVIC J, BROZ P, PICHA R. Microstructural and phase equilibria study in the Ni–Al–Cr–W system at 1173 and 1273 K [J]. Intermetallics, 2003, 11: 483–490.
- [23] LLEWELYN S C H, CHRISTOFIDOU K A, ARAULLO-PETERS V J, JONES N G, HARDY M, MARQUIS E, STONE H J. The effect of Ni:Co ratio on the elemental phase partitioning in γ - γ' Ni–Co–Al–Ti–Cr alloys [J]. Acta Materialia, 2017, 131: 296–304.
- [24] WAGNER C. Passivity and inhibition during the oxidation of metals at elevated temperatures [J]. Corrosion Science, 1965, 5: 751–764.
- [25] YANG X, PENG X, XU C, WANG F. Electrochemical assembly of Ni–xCr– γ Al nanocomposites with excellent high-temperature oxidation resistance [J]. Journal of The Electrochemical Society, 2009, 156: 167–175.
- [26] NIU Y, ZHANG X J, WU Y, GESMUNDO F. The third-element effect in the oxidation of Ni–xCr–7Al (x=0, 5, 10, 15 at.%) alloys in 1 atm O₂ at 900–1000 °C [J]. Corrosion Science, 2006, 48: 4020–4036.
- [27] NIU Y, WANG S, GAO F, ZHANG Z G, GESMUNDO F.

- The nature of the third-element effect in the oxidation of Fe-xCr-3at.%Al alloys in 1 atm O₂ at 1000 °C [J]. Corrosion Science, 2008, 50: 345–356.
- [28] HUTCHINSON J W, HE M Y, EVANS A G. The influence of imperfections on the nucleation and propagation of buckling driven delaminations [J]. Journal of the Mechanics and Physics of Solids, 2000, 48: 709–734.
- [29] LI M H, SUN X F, HU W Y, GUAN H R, CHEN S G. Hot corrosion of a single crystal-Ni-base superalloy by Na-salts at 900 °C [J]. Oxidation of Metals, 2006, 65: 137–150.
- [30] GOWARD G. Protective coatings-purpose, role, and design [J]. Material Science Engineering, 1986, 2: 194–200.

Co 对两种镍基高温合金 900 °C 氧化和 Na₂SO₄-NaCl 盐热腐蚀行为的影响

孟君晟, 陈明宣, 史晓萍, 马强

山东交通学院 船舶与港口工程学院, 威海 264200

摘 要: 采用双真空熔炼法, 通过部分置换 W 制备含 Co 和不含 Co 的镍基高温合金。系统研究合金在 900 °C 下的氧化与 75%Na₂SO₄+25%NaCl(质量分数)熔盐热腐蚀行为。结果表明, Co 部分置换 W 促进 Cr₂O₃ 的形成, 从而降低氧化速度; 此外, Co 抑制 Al 的内氧化和内氮化, 促进 Al₂O₃ 膜的快速形成, 从而进一步降低氧化速度, 提高氧化膜的抗裂性能。此外, Co 可以进一步提高合金在 Na₂SO₄-NaCl 熔盐下的热腐蚀性能。

关键词: 镍基高温合金; 氧化; 热腐蚀; 抗剥落性

(Edited by Xiang-qun LI)